

RESEARCH ARTICLE

10.1002/2014JE004671

Key Points:

- Depth/diameter ratio for new, dated, meter-scale craters on Mars averages 0.23
- Fresh-appearing lunar craters of similar size have $d/D \sim 0.10$
- New meter-scale craters are recognizable as primaries from their d/D ratios

Supporting Information:

- Readme
- Figure S1
- Table S1
- Table S2
- Table S3

Correspondence to:

I. J. Daubar,
ingrid@lpl.arizona.edu

Citation:

Daubar, I. J., C. Atwood-Stone, S. Byrne, A. S. McEwen, and P. S. Russell (2014), The morphology of small fresh craters on Mars and the Moon, *J. Geophys. Res. Planets*, 119, 2620–2639, doi:10.1002/2014JE004671.

Received 21 MAY 2014

Accepted 5 NOV 2014

Accepted article online 10 NOV 2014

Published online 17 DEC 2014

The morphology of small fresh craters on Mars and the Moon

Ingrid J. Daubar¹, C. Atwood-Stone¹, S. Byrne¹, A. S. McEwen¹, and P. S. Russell²

¹Lunar and Planetary Laboratory, University of Arizona, Tucson, Arizona, USA, ²Center for Earth and Planetary Studies, Smithsonian Institution, Washington, District of Columbia, USA

Abstract The depth/diameter ratio for new meter- to decameter-scale Martian craters formed in the last ~20 years averages 0.23, only slightly deeper than that expected for simple primary craters on rocky surfaces. Large variations in depth/diameter (d/D) between impact sites indicate that differences between the sites such as target material properties, impact velocity, angle, and physical state of the bolide(s) are important in determining the depth of small craters in the strength regime. On the Moon, the d/D of random fresh small craters with similar diameters averages only 0.10, indicating that either the majority of them are unrecognized secondaries or some proportion are degraded primaries. Older craters such as these may be shallower due to erosional infilling, which is probably not linear over time but more effective over recently disturbed and steeper surfaces, processes that are not yet acting on the new Martian craters. Brand new meter- to decameter-scale craters such as the Martian ones studied here are statistically easily distinguishable as primaries, but the origins of older craters of the same size, such as the lunar ones in this study, are ambiguous.

1. Introduction

Several hundred new impact sites on Mars have been discovered [Daubar *et al.*, 2013] and confirmed by the High Resolution Imaging Science Experiment (HiRISE) [McEwen *et al.*, 2007] following their discovery by the Context camera [Malin *et al.*, 2007], both on the Mars Reconnaissance Orbiter. The new craters are exceptionally small, ranging from ~40 m in diameter down to just a few meters, with some even smaller craters that cannot be resolved. These impact events have occurred within the last few decades, sometimes within the last few months, as indicated by the absence of associated impact-related dark surface markings in previous images.

These new small craters are all almost certainly primaries because they formed at different times, in widespread locations across the planet (Figure 1). No new craters have been found that could be the potential primary. First of all, the formation times of nearly all of the new craters are constrained to have occurred within nonoverlapping time periods, such that their formations cannot be simultaneous. The statistical probability of multiple new large impact events occurring within the last decade to explain all of these with separate secondary-forming events is extremely low. Second, the new craters are too large. The largest secondaries produced by a given crater are ~4% the diameter of the primary [Allen, 1979; Schultz and Singer, 1980]. Thus, a hypothetical primary that produced ~1–30 m secondaries would be ~25–750 m in diameter. While a few new craters are in the ~20–30 m diameter range, their times of formation are not consistent with being the source crater for any of the new impacts. None have been discovered larger than 50 m. New craters >100 m diameter would almost certainly have been detected by at least one of the eight cameras orbiting Mars on four spacecraft over the past decade.

Statistics of small primary impact events constrain surface modification rates [e.g., Banks *et al.*, 2010; Golombek *et al.*, 2010] and have important implications for the broader field of planetary chronology [e.g., McEwen *et al.*, 2005; McEwen and Bierhaus, 2006; Hartmann, 2007]. The difficulty has been in distinguishing small primaries from the secondaries produced episodically and nonrandomly in both space and time by larger primaries [Shoemaker, 1965]. It has been suggested that most of the small craters in many regions of Mars are secondaries based on the large number of secondaries from Zunil crater (age estimated as ~0.1 to <100 Ma [McEwen *et al.*, 2005; Hartmann *et al.*, 2010; Williams *et al.*, 2014]), which have depth/Diameter (d/D) ratios ~0.08 [McEwen *et al.*, 2005] up to 0.15–0.20 in some places [Watters and Radford, 2014]. With a measured current production function [Daubar *et al.*, 2013], we now know the rate at which small primaries are forming. One possible explanation for the difference between that measured rate and the model production functions of Neukum *et al.* [2001], Ivanov [2001], and Hartmann [2005] could be

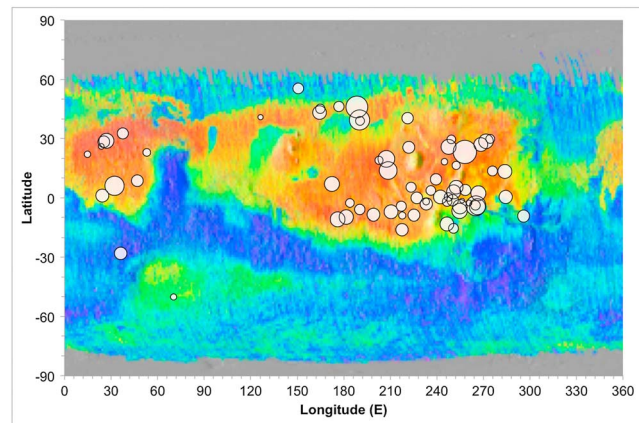


Figure 1. Locations of 72 new dated impact sites on Mars included in the shadow measurement study, shown on a map of the Thermal Emission Spectrometer dust cover index [Ruff and Christensen, 2002]. Width of circles is proportional to depth/diameter ratio at that site (averaged where multiple craters in a simultaneously formed cluster were measured).

the inclusion in those models of unrecognized secondaries. This might allow for a measurement of the relative numbers of primaries and secondaries at small diameters. However, the size of the contribution of secondary craters to crater size frequency distributions (SFDs) on older surfaces is still uncertain, and several other possible explanations exist for the mismatch between measured and model SFDs (see Daubar *et al.* [2013] for discussion). Thus, the relative numbers of small primaries and secondaries are still not understood. We therefore investigate the morphologies of these new Martian primaries and, for comparison, random small craters on the Moon whose primary or secondary origin is unknown, and where the atmospheric variable is eliminated.

The ratio of rim-to-floor depth to rim diameter (d/D) has been widely presented as a simple description of the shape of craters. Power laws have also been used of the form $d = c_1 D^{c_2}$, which have the advantage of accommodating poor-fitting linear relations when c_2 is far from 1. Less common is a polynomial form, as used by Baldwin [1985]. Although none of these models may be physically justified, and a more complex model may be a better fit to the data [Mahanti *et al.*, 2013], we present our data here in the linear and power law forms for comparison with previous work.

Typical d/D has long been known to be ~ 0.2 for primary simple craters on the Moon [e.g., Pike, 1974, 1977; Wood and Anderson, 1978], Mars [e.g., Pike, 1980; Cintala and Mouginis-Mark, 1980], and Mercury [Barnouin *et al.*, 2012]. Secondaries, on the other hand, are shallower [Shoemaker, 1965], with $d/D \sim 0.1$ [e.g., Pike and Wilhelms, 1978; Schultz and Singer, 1980; McEwen *et al.*, 2005]. The large amount of variation in the best fit trends to d/D may be due to the inadvertent inclusion of secondaries and/or degraded craters, resolution or measurement errors, or varying target or impact properties. These relationships are almost all based on larger craters than the very small ones in this study, however, underscoring the motivation and importance of investigating morphologies at these small sizes.

Determining whether a crater is a primary or a secondary is difficult when a secondary is far from its primary. Such distant secondaries are formed by impact of ejecta at high velocity, forming circular, isolated small craters that may have no obvious connection to their primary. Criteria used for identifying secondaries are not always present or reliable. Noncircularity, for example, while secondaries can deviate from circular [e.g., Pike and Wilhelms, 1978], so can oblique primary impacts. Distant secondaries can also be circular because the impact velocity must be high [McEwen *et al.*, 2005; Tornabene *et al.*, 2006; Calef *et al.*, 2009]. Observations of regional crater ejecta characteristics and asymmetries are another way to identify well-preserved secondaries [Calef *et al.*, 2009; Wells *et al.*, 2010]; however, ejecta of small craters erode rapidly, leaving no sign of the original ejecta morphology. These also may be indistinguishable from highly oblique primary impacts. Secondaries often form in clusters, but clustering alone cannot be used to recognize secondaries: observations [Daubar *et al.*, 2013] and modeling [Popova *et al.*, 2007] show that small primary impactors fragment in the Martian atmosphere, creating clusters of primary craters. Optical or infrared detection of rays are also used in identifying secondaries contained within them [McEwen *et al.*, 2005; Tornabene *et al.*, 2006], but the rays are not always present or preserved.

None of these distinguishing characteristics is either universal or unqualified. For this reason, being able to determine the provenance of craters based on their morphology would be advantageous. Despite its wide variation, d/D has long been used as a criterion for distinguishing primary from secondary craters [e.g., Golombek *et al.*, 2006].

From several years of Mars Reconnaissance Orbiter observations, we now have a data set of small craters that we know are extremely fresh primaries. Their d/D ratios can be used as a standard for studies of craters whose origin is not as clear, for example, those spatially random craters that could be either primaries or distant secondaries.

Because distant secondaries impact at higher velocity than secondaries close to their primary, one might suspect that these distant secondaries will also have higher d/D , closer to that of primaries. There is an indication of such a trend in secondaries from Zunil and Gratteri craters on Mars [Watters and Radford, 2014]. (Wilcox *et al.* [2005] also stated that distant secondaries of Tycho Crater have $d/D \sim 0.2$ based on the observation that shadows extend halfway across the crater at an incidence angle of 79° . We note, however, that this was an error, and the correct d/D matching this observation is ~ 0.1 .) In fact, however, experimental work [Schultz, 1989; Barnouin *et al.*, 2011] shows that the opposite should occur, at least in transient craters: lower velocity impacts (whether primary or secondary) produce relatively deeper craters with higher d/D . Recent modeling by Bray and Schenk [2014] indicates that this trend is weaker the smaller the projectile, so very small craters such as the ones we are studying may in fact not show a strong variation in d/D with impact velocity, i.e., secondary distance from the primary. In any case, the typically observed lower d/D of secondaries compared to primaries is borne out by observations but is still largely unexplained.

2. Methods

2.1. Shadow and Diameter Measurements

We measured new craters in HiRISE Reduced Data Record (RDR) images to obtain rim-to-rim diameter and rim-to-floor depth using the shadow measurement technique of Chappelow and Sharpton [2002]. They derived formulae for crater depths based on shadow lengths that depend on crater shape (parabolic, conical, or flat floored), which can be determined based on the shape of the shadow falling on the crater floor. This method has been shown to give reliable depths for smaller craters than either altimetric or stereo measurements, which are only available at lower resolutions [Herrick, 2013]. This technique is particularly useful because it does not require a specific incidence or viewing angle; the shadow edge does not have to intersect the deepest point of the crater to calculate the crater's maximum depth. It does require a distinct shadow (an example lacking this is shown in Figure 2c) and a supposition about the crater's three-dimensional form based on the shadow edge shape; uncertainties in either of these lead to errors. While Chappelow [2013] has recently generalized the method to a crater with any conic section surface of revolution, that level of precision was not determined to be necessary. In addition, Barnouin *et al.* [2012] found the results of the two methods to be indistinguishable.

All HiRISE images used are listed in Table S1 in the supporting information. Measurements were made using the image processing software package ENvironment for Visualizing Images (ENVI) and analyzed using Interactive Data Language (IDL) (<http://www.exelisvis.com/>). Features that were too small to be confidently measured (<4 pixels across), craters with indistinct or uneven rims, unclear shadows, or concentric "nested" rims (Figure 2) were excluded from the study. We used a lower limit of 2.5 m diameter, since the shadow technique has been found to give reasonable depths for craters with diameters larger than 10 times the pixel scale [Herrick, 2013]. HiRISE's three-band color coverage was useful for distinguishing shadows from dark material when it was occasionally exposed in the interiors of craters, as the dark material is typically less red than shadows.

Calculation of depth using this method depends on a determination of crater profile morphology (parabolic, flat floored, or conical) based on the shadow shape [Chappelow and Sharpton, 2002]. There is quite a bit of uncertainty in the crater profile determination, since most of the shadows subtend so few pixels that resolving a shape is difficult. Only 29% of craters could be assigned a probable profile (10% parabolic, 10% conical, and 9% flat floored). We used the depth calculation appropriate for the crater profile as determined by shadow shape, when it could be determined; when it could not, we assumed a conical shape. This is because conical, or "V-shaped" craters, are the most common shape at small sizes on the Moon [Stopar *et al.*, 2012; Chappelow, 2014]. In addition, two out of the three craters where we have three-dimensional data (section 2.2) have conical profiles (the third is roughly parabolic). Third, we found a correlation between incidence angle and measured d/D at low incidence angle, which was strongest when a parabolic shape was assumed (Figure 8a) and weakest when

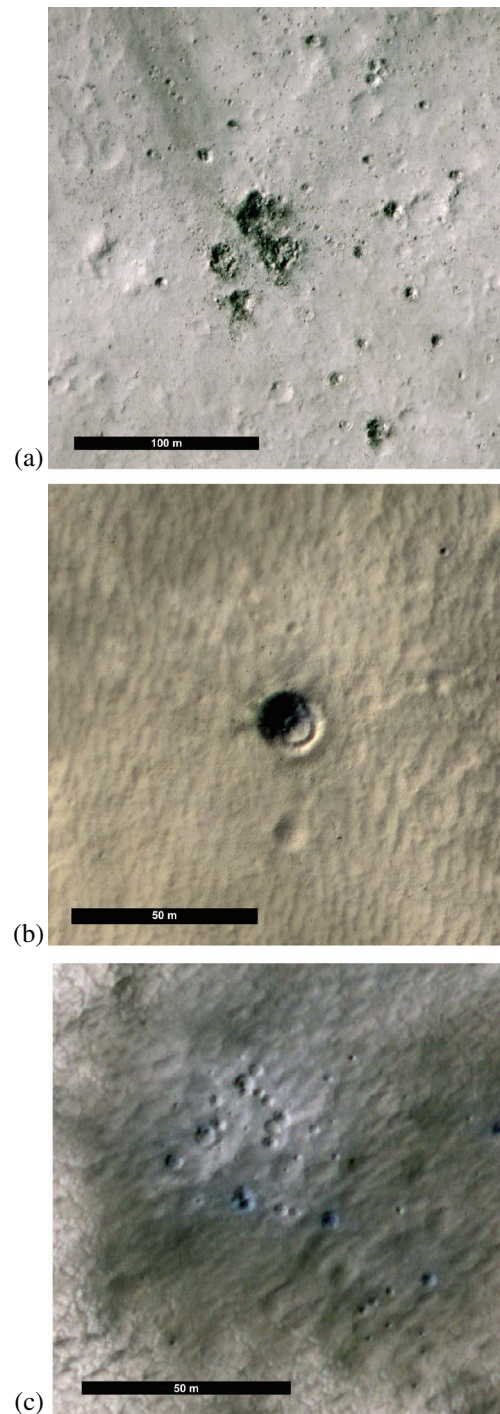


Figure 2. Examples of new impact sites on Mars whose depths cannot be measured using the shadow measurement technique because (i) craters are too shallow/irregular; (ii) craters are “nested,” with concentric benches or terraces; or (iii) solar incidence angle is less than the cutoff of 55° (in this case $i = 44.7^\circ$), so shadows are inadequate or indefinite. (a) HIRISE observation ID PSP_007499_1810, 0.933°N , 191.746°E . (b) ESP_017447_1785, -1.326°N , 30.780°E . (c) ESP_026009_1920, 11.825° , 275.702°E . Images are sections of COLOR RDRs (IRB color, stretched for contrast), North is up, and the scene is illuminated from the upper left. Image credits: NASA/JPL/University of Arizona.

assuming a conical shape (Figure 8b). Variation in d/D when assuming different shapes is only $\sim 10\%$ on average, so assuming a conical profile when shape could not be determined is not a large source of error. We also used the incidence angle dependence (Figure 8a) to choose a minimum solar incidence angle of 55° in order to exclude sites with inadequate shadows. The bright sky light from Mars’ dusty atmosphere makes shadows less distinct than on atmosphereless bodies, so distinguishing shadows from obliquely illuminated (shaded) slope areas is difficult at small incidence angles and consequent small or absent shadows (e.g., Figure 2c).

The edges of shadows were determined by overlaying contour lines of Density Number (DN) level. The location where the lines were most closely spaced was taken to be the shadow edge; this location does not change when contrast stretching or similar image processing is applied. An example of a site with inadequate shadows, where this method could not be used, is shown in Figure 2c.

Since the images used were taken at different viewing angles (emission angles ranged from 0.35° to 9.4°), small corrections were made for the distortions in apparent shadow length due to varying emission angles according to *Barnouin et al.* [2012]. In addition, we rederived their correction for viewing azimuth angle with slightly different results, as detailed in Appendix A, and we applied this new correction to our measurements. This had a small effect: the absolute value of the difference in depth due to this correction averaged only 5.3%, with a maximum of 17%; only 12% of the craters had a correction that amounted to more than 10% of the absolute value of the difference in depth.

The uncertainty on individual measurements is high, since some features such as the crater rim or details of the shadow edge shape are not much larger than the image resolution (2–3 pixels); each measurement was taken 3 times and averaged to partially address this. Error bars in Figure 4 and Table S1 are for diameters: the standard deviation between the three measurements; for depths: the standard deviation between the depths calculated using the three shadow measurements and using the depth calculation appropriate for the individual crater’s shape.

Best fit power laws for all sets of data were calculated using the least squares method in IDL using Gaussian weighting of $1/(d_{\text{err}})^2$, where d_{err} is the standard deviation between depths calculated from the three shadow length measurements.

2.2. Martian DTM Measurements

Three Digital Terrain Models (DTMs) of the dated impact sites were produced by the University of Arizona using HiRISE stereo imagery [Kirk *et al.*, 2008; Mattson *et al.*, 2011]. The image pairs are ESP_012282_1775 and ESP_011425_1775 (centered at 2.364°S, 278.264°E); ESP_025152_1945 and ESP_025007_1945 (14.523°N, 268.849°E); and ESP_032881_1855 and ESP_032736_1855 (5.457°N, 224.356°E).

The DTMs were imported into ENVI using the HiRISE Toolkit. An elliptical region of interest (ROI) was fit visually to the crater rim as represented by the highest elevation points around the crater. The mean of elevation points along a transect that traces that ellipse was used as the rim height; subtracting the minimum elevation value within the ROI yielded the depth of the crater. The crater's mean diameter D was calculated from the ROI area A from $D = 2\sqrt{A/\pi}$. Error bars shown in Figure 4 are for diameters: one horizontal DTM post distance (1 m in these cases); and for depths: the estimated vertical precision. This was calculated according to Kirk *et al.* [2003] as $\Delta p \times \text{IFOV}/\tan \theta$, where Δp is the subpixel matching quality; IFOV is the Instantaneous Field Of View, which in this case was the average pixel scale of the original source nonmap-projected data; θ is the stereo convergence angle, the tangent of which is used to approximate the value of parallax/height. For θ we used the sum of the emission angles of the two images used to make the DTM, if the two images were taken from opposite sides; or the difference in emission angles, if they were taken from the same side. The resulting vertical precisions range from ~0.1–0.5 m for these particular DTMs.

DTM measurement results for Martian craters are shown in Figure 4. We could in some cases compare measurements made on the DTMs to the shadow measurements made on visual images. Diameters from both methods are very similar, averaging 4% different. The depth could not be measured using the shadow technique at the sites of ESP_012282_1775/ESP_011425_1775 or ESP_025152_1945/ESP_025007_1945 due to irregular, shallow floors. The techniques could be compared at the third site, ESP_032881_1855/ESP_032736_1855, although the highest incidence angle image at that site, PSP_004030_1855, had $i = 54.95^\circ$, just barely below the cutoff we use in this analysis. In that case, the depths differed by 1.2 m or 13%, and d/D differed by 9%. This gives an idea of the variation between techniques.

Note that due to the large estimated vertical precision relative to the shallow depth of the crater at site ESP_025152_1945/ESP_025007_1945, we do not consider this measured d/D to be very reliable.

2.3. Lunar DTM Measurements

Diameters and depths of lunar craters were measured in two DTMs made from images taken by the Lunar Reconnaissance Orbiter (LROC) Narrow Angle Camera (NAC) [Robinson *et al.*, 2010]. The first DTM is located near the Apollo 15 landing site using the NAC images M111571816 and M111578606 (26.06°N, 3.60°E); the second is at Mare Ingenii using the NAC images M141187604 and M141194388 (−35.55°N, 164.73°E). The particular regions for measurement were chosen specifically to avoid obvious secondaries such as those appearing in crater chains and clusters. In addition, craters that were noticeably elliptical were not included, as they are more likely to be secondaries.

Craters were measured using ArcMap and the Crater Helper Tools add-on. The lowest point within each crater was taken as the lowest elevation in the cropped portion of the DTM. The average rim elevation of each crater was visually estimated. The diameter of these rims were measured using the three-point circle tool, a feature of the Crater Helper Tools add-on, which allowed us to place three points on the obvious portions of the crater rim to find the diameter of the circle they describe.

A subset of the measured lunar craters was further categorized in terms of relative freshness of the craters. The criteria used in making these determinations were primarily the relative brightness of the ejecta and the relative sharpness of the crater rims. Craters assigned to freshness level one (the most fresh) were obvious in both the DTM and the visible image, with high albedo both within the crater itself and ejecta that is brighter than the surrounding terrain. Craters in level two (medium fresh) were still obvious in both the DTM and the visible images but lacked an albedo distinct from their surroundings. Craters judged to be in level three (least fresh) were low-albedo features: the craters are almost completely undefined in visible images, being obvious only in the DTM.

Error bars for the DTMs were calculated using the same method as above. The LROC DTMs both have horizontal postings of 2 m. The smallest craters in this study (minimum crater diameter of 17 m) are well resolved by these high-resolution DTMs and is similar to the 20 m minimum used by Basilevsky *et al.* [2014].

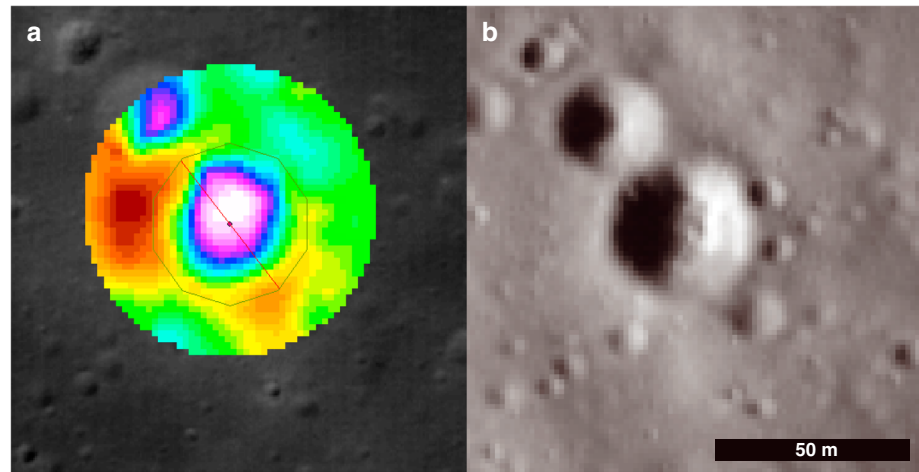


Figure 3. Example of a crater used for comparison between (i) DTM and (ii) shadow measurement techniques, with respective measurements. Lunar crater located at 26.267°N, 3.651°E. (a) DTM created from LROC NAC images M111571816 and M111578606. DTM cutout overlain on background orthoimage NAC_DTM_APOLLO15_M111571816_50 cm. cub shown for context. In the DTM, red is high and white is low. The scale bar shows color-coded elevations in meters relative to the lunar datum, spanning a total vertical distance of 6.3 m; the 32 colors are scaled using the natural breaks (Jenks) algorithm in ArcGIS. Measured diameter 40.1 m; depth 5.4 m; d/D 0.13. (b) LROC NAC image M1111791841 with solar incidence angle 72.4°. Measured diameter 38.3 m; depth 5.4 m; d/D 0.14. This crater was categorized as having a flat floor based on the shadow edge shape; the DTM confirms that shape.

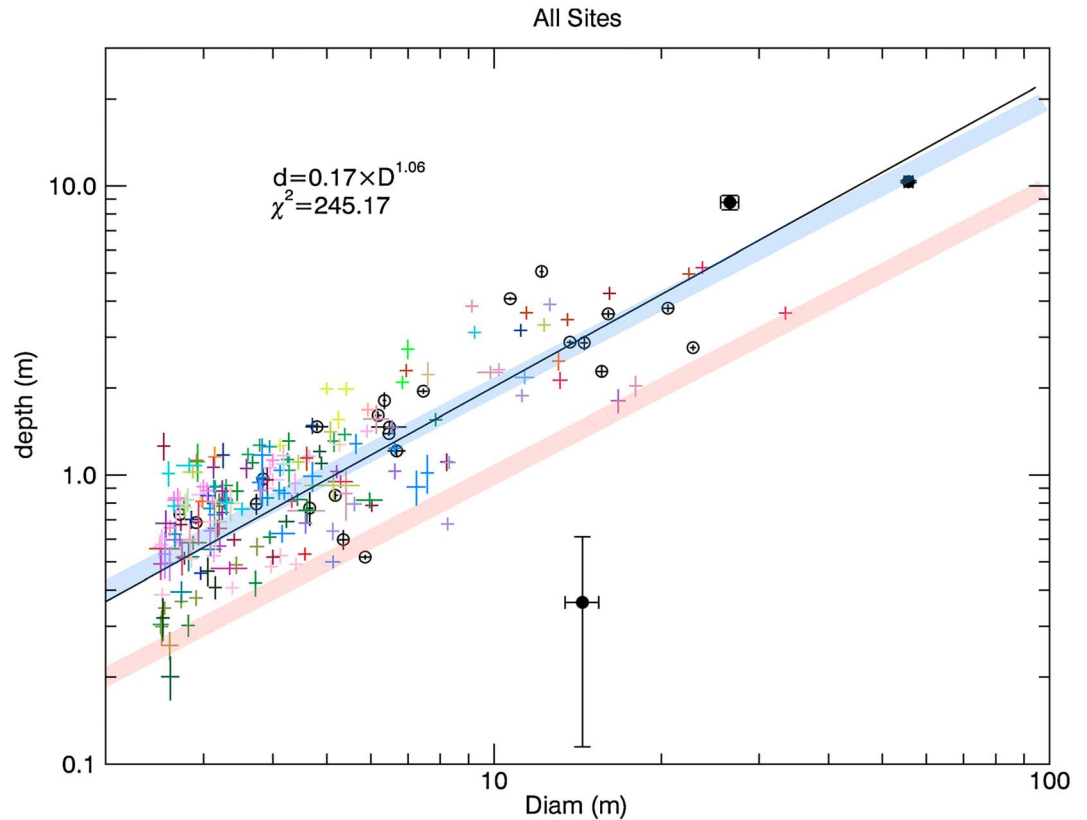


Figure 4. Diameter (D , in meters) plotted versus depth (d , in meters) of recent dated Martian impact sites. Crosses and open circles are measurements made using the shadow measurement technique. For clusters of multiple craters at the same site, all craters at the same site are shown in the same color. Open circles represent single-crater sites. A least squares power law fit (solid black line) was made to all individual shadow measurement points, using weights of $1/(d_{err})^2$. Filled black circles are measurements made on digital terrain models. Trends of $d/D = 0.1$ (light red line) and 0.2 (light blue line) are also shown for comparison.

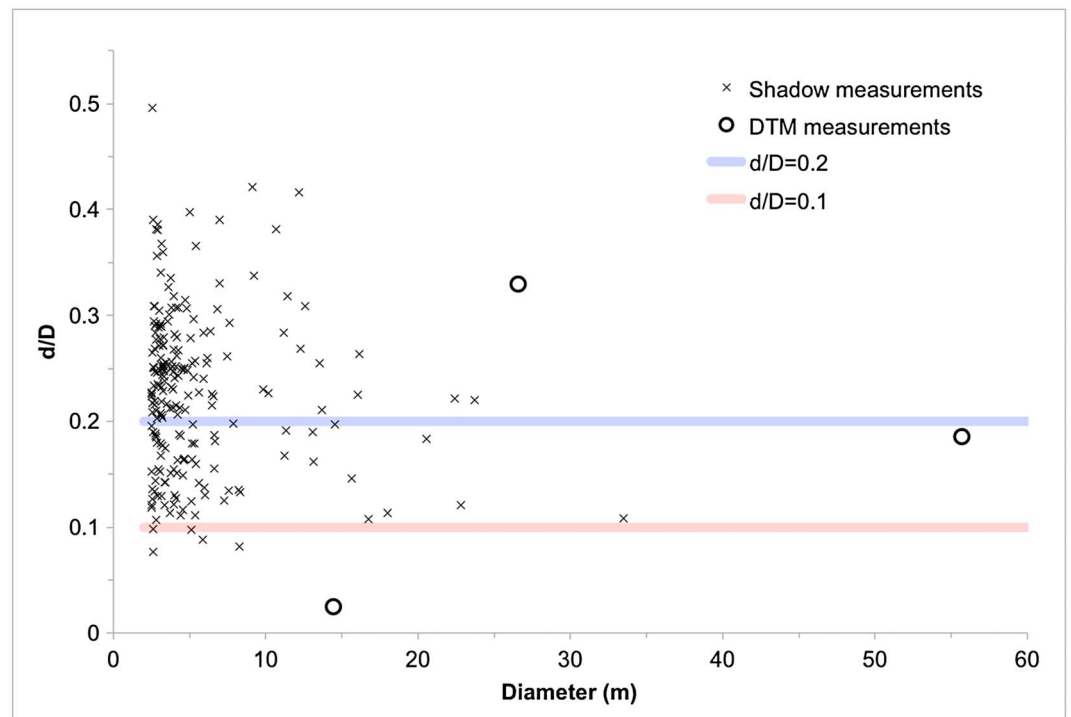


Figure 5. Depth/Diameter (d/D) plotted against diameter (in meters) for each Martian crater measured. Open circles mark measurements made on Digital Terrain Models; those marked with a cross symbol were made using the shadow measurement technique. Trends of $d/D = 0.1$ (light red line) and 0.2 (light blue line) are also shown for comparison.

Lunar crater diameters range from 17 to 919 m, so although most of these craters are larger than the Martian ones in this study, the ranges do overlap.

2.4. Comparison of Techniques on the Same Data Set

To calibrate the two techniques, 10 lunar craters were selected from a lunar DTM and also measured using the shadow measurement technique (Figure 3). At incidence angles $>55^\circ$, which is the limit we used in our shadow measurements, the average of the absolute value of the differences in d/D was only 15%, so we have some confidence that the two measurement techniques yield comparable results.

3. Results

3.1. Martian Primary Craters

After discarding observations deemed unsuitable according to the above criteria, 209 craters at 72 impact sites remained, ranging from 2.5 to 34 m in diameter. All Martian measurements are presented in Table S1 of the supporting information. These are plotted on a base map of the Thermal Emission Spectrometer Dust Cover Index (DCI) [Ruff and Christensen, 2002] (Figure 1). This shows that, although there is a spatial bias in our data set toward the dustiest areas of Mars due to the detection technique [Daubar et al., 2013], the average d/D at each site does not necessarily correspond to the DCI value at that site.

The average d/D over all craters is 0.228 ± 0.005 . Figures 4 and 5 show a plot of $\log(\text{depth})$ versus $\log(\text{Diameter})$ for each crater; single-crater sites are plotted as circles, while multiple-crater sites are plotted with one cross symbol for each crater in the cluster, using the same unique color for each site. The least squares power law fit to all individual craters is $d = 0.17D^{1.06}$.

There appears to be no dependence of d/D on emission angle (Figures 6 and 7), as expected as the maximum emission angle used is only 9.4° , and we apply a correction for nonzero emission angles (Appendix A).

Most (74%) craters' measured d/D values are higher than the maximum possible d/D of 0.175 that could be achieved in a parabolic crater with maximum steepness at a dynamic angle of repose of 35° (we calculate this maximum to be 0.175, rather than the 0.19 value stated in Guskova et al. [2013]). Dynamic angles of

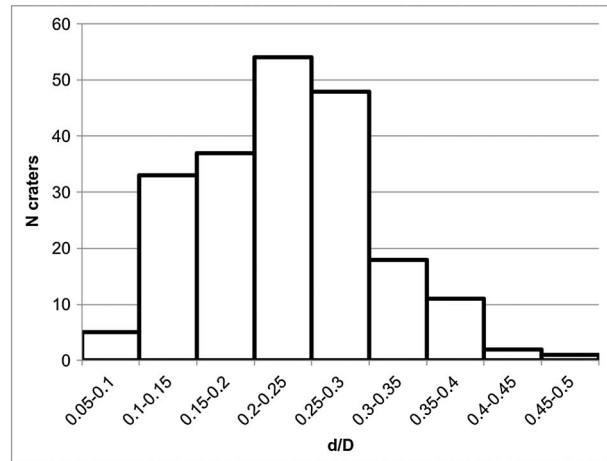


Figure 6. Histogram of all d/D values measured on Mars with the shadow measurement technique, showing a broad range of values with a peak 0.2–0.3.

repose measured from Martian dune field slip faces range from 32 to 35° [Atwood-Stone and McEwen, 2013]. These results suggest that these craters are for the most part not parabolic in shape, supporting our default use of the conical shape (which allows d/D of up to 0.35 in unconsolidated material).

We also investigated d/D trends on a site-by-site basis, looking at only those sites with clusters of three or more measurable craters (Figures 8 and 9 and Figure S1 in the supporting information). Power laws of the form $d = c_1 D^{c_2}$ were fit to the entire group of individual craters within each cluster. The resulting coefficients range widely (Table S3 in the supporting information) most likely because of small

number statistics. Nevertheless, average d/D values for the sites tend to fall above the 0.2 trend line (Figure S1 and Table S3): 68% of sites have average $d/D > 0.2$, and the average of all the site averages is 0.233 ± 0.013 .

3.2. Lunar Craters of Unknown Origin

The average d/D for the 554 lunar craters measured is 0.096 ± 0.0012 (Figure 10). All lunar measurements are presented in Table S2. The least squares best power law fit for the craters at the Apollo 15 landing site is $d = 0.07D^{1.05}$ and at the Mare Ingronii site is $d = 0.06D^{1.06}$.

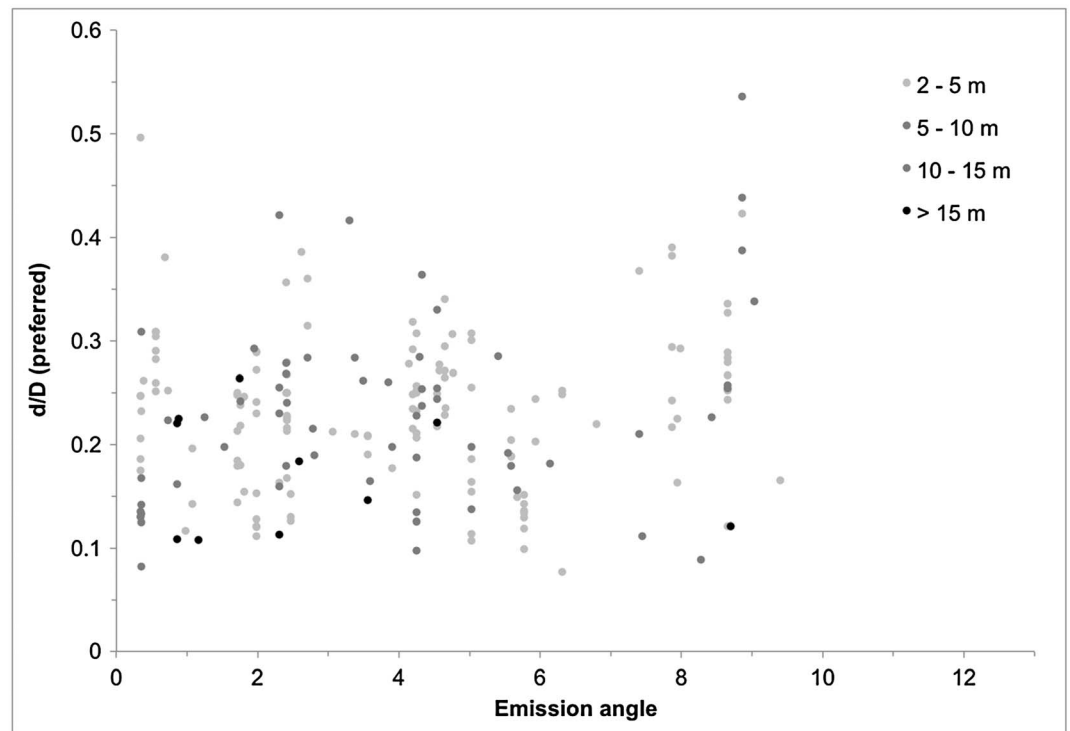


Figure 7. Values of d/D from the shadow measurement technique as a function of emission angle of the image, using the preferred shape for each crater when it could be determined, otherwise using conical as the default. Assuming any single shape for all shows a similar lack of dependence on emission angle. Points are shaded according to crater diameter, from the lightest gray for the smallest craters to black for the largest craters.

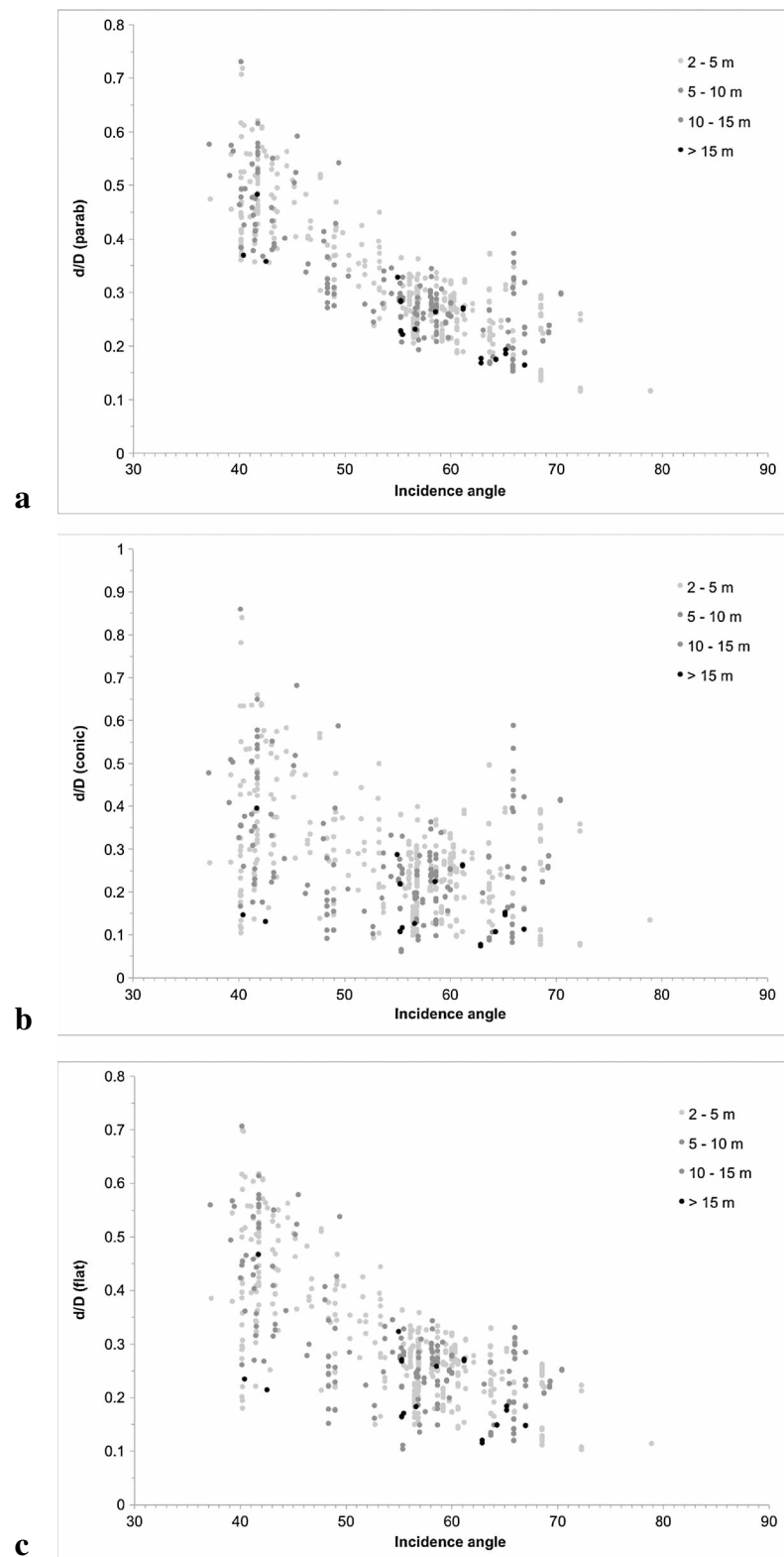


Figure 8. Values of d/D from the shadow measurement technique as a function of the incidence angle of the image in which the measurements were taken, assuming (a) parabolic, (b) conic, and (c) flat-floored craters. Incidence angles less than 55° are shown to demonstrate the dependence on incidence angle for lower values; the analysis in this paper included only images with incidence $>55^\circ$ for this reason. Points are shaded according to crater diameter, from the lightest gray for the smallest craters to black for the largest craters.

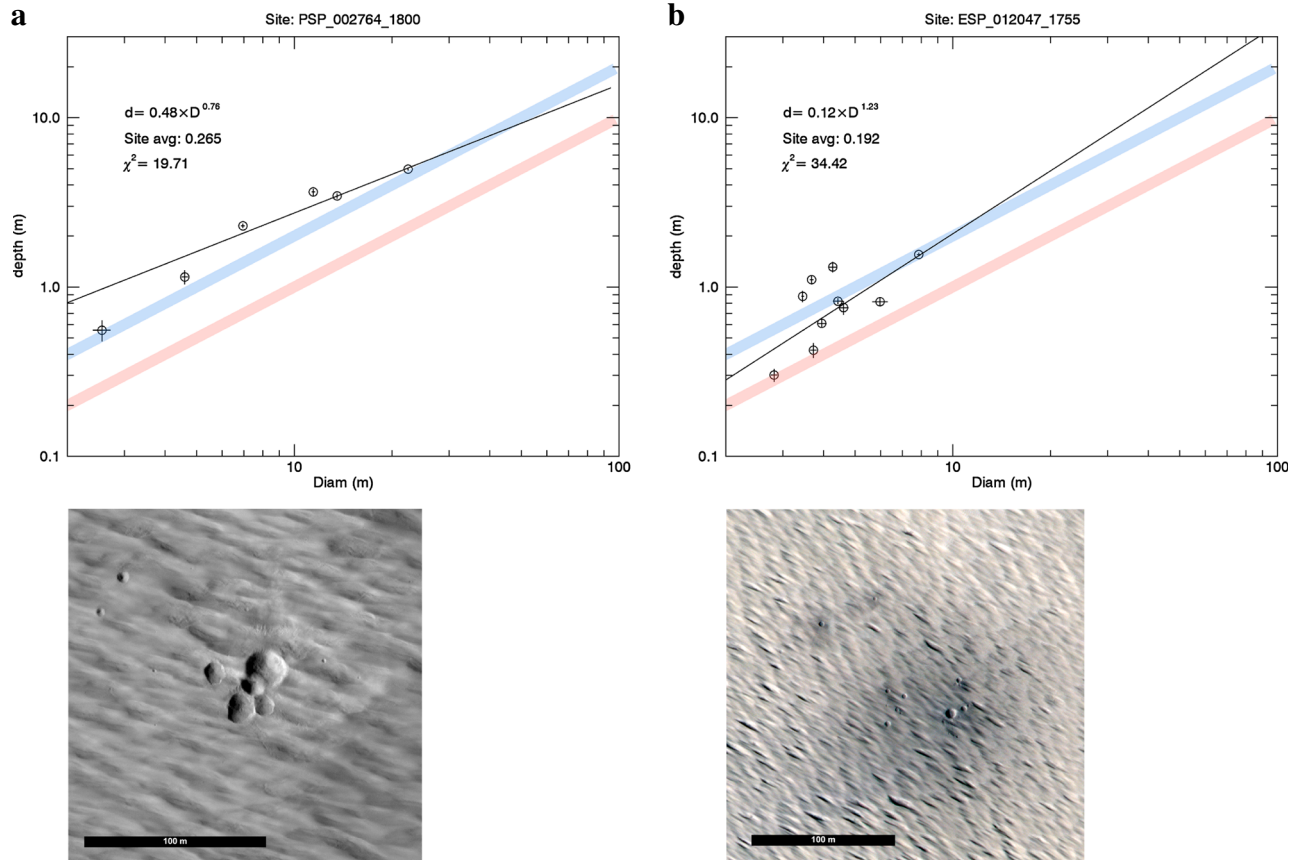


Figure 9. Examples of d/D power law fits for groups of clustered craters at several different new Martian impact sites, plotted as in Figure 4. Plots such as these for all sites with three or more measured craters are shown in Figure S1. Images are cutouts from RDRs (RED or COLOR, stretched for contrast), North is up, and the scene is illuminated from the upper left. Image credits: NASA/JPL/University of Arizona. (a) PSP_002764_1800 at -0.033°N , 226.907°E (RED). At this site, d/D is fairly consistent among craters with a wide range of diameters. Values of d/D measured at this site range from 0.21 to 0.33. (b) ESP_012047_1755 at -4.375°N , 217.120°E (COLOR). At this site, d/D has a wide range of values within the same cluster. Values of d/D measured at this site range from 0.11 to 0.31.

When craters were separated by apparent freshness (Figure 11), the freshest-looking craters (freshness level 1) have the highest d/D ratios, but freshness levels 2 and 3 (medium and least fresh) have overlapping values within the error bars. For freshness level 1, the average d/D is 0.102 ± 0.020 (seven craters); for freshness level 2, the average d/D is 0.090 ± 0.007 (17 craters); and for freshness level 3, the average d/D is 0.096 ± 0.006 (22 craters). The trend of depth with freshness is also reflected in the power law fits: $d = 0.095D^{1.07}$ (freshness level 1); $d = 0.010D^{1.59}$ (freshness level 2); and $d = 0.005D^{1.51}$ (freshness level 3). As might be expected, the depth decreases monotonically with decreasing freshness in the size range we are studying. For example, for a hypothetical 50 m diameter crater following these power law trends, the depths would be as follows: 6.2 m (freshness level 1), 5.0 m (freshness level 2), and 1.8 m (freshness level 3).

4. Discussion

4.1. Comparison to Other Primary Craters

Primary simple craters on rocky planets typically have $d/D \sim 0.2$ [e.g., Pike, 1974, 1977, 1980; Schultz and Singer, 1980; Garvin et al., 2003; Barnouin et al., 2012]. The average d/D we measure of fresh Martian craters of 0.23 is quite close to that, although a significant number of them are higher than typical: 64% of the craters in our study have $d/D > 0.2$. There is a slight tendency for larger craters to have smaller d/D , although that variation is within the spread of our data. It should be noted that the very shallowest of craters (e.g., Figure 2a), perhaps created by highly decelerated impactors, cannot be measured using the shadow technique except with very high incidence angle images, which are rare. So we expect that our data set is slightly skewed toward craters with higher d/D . This technique also cannot be

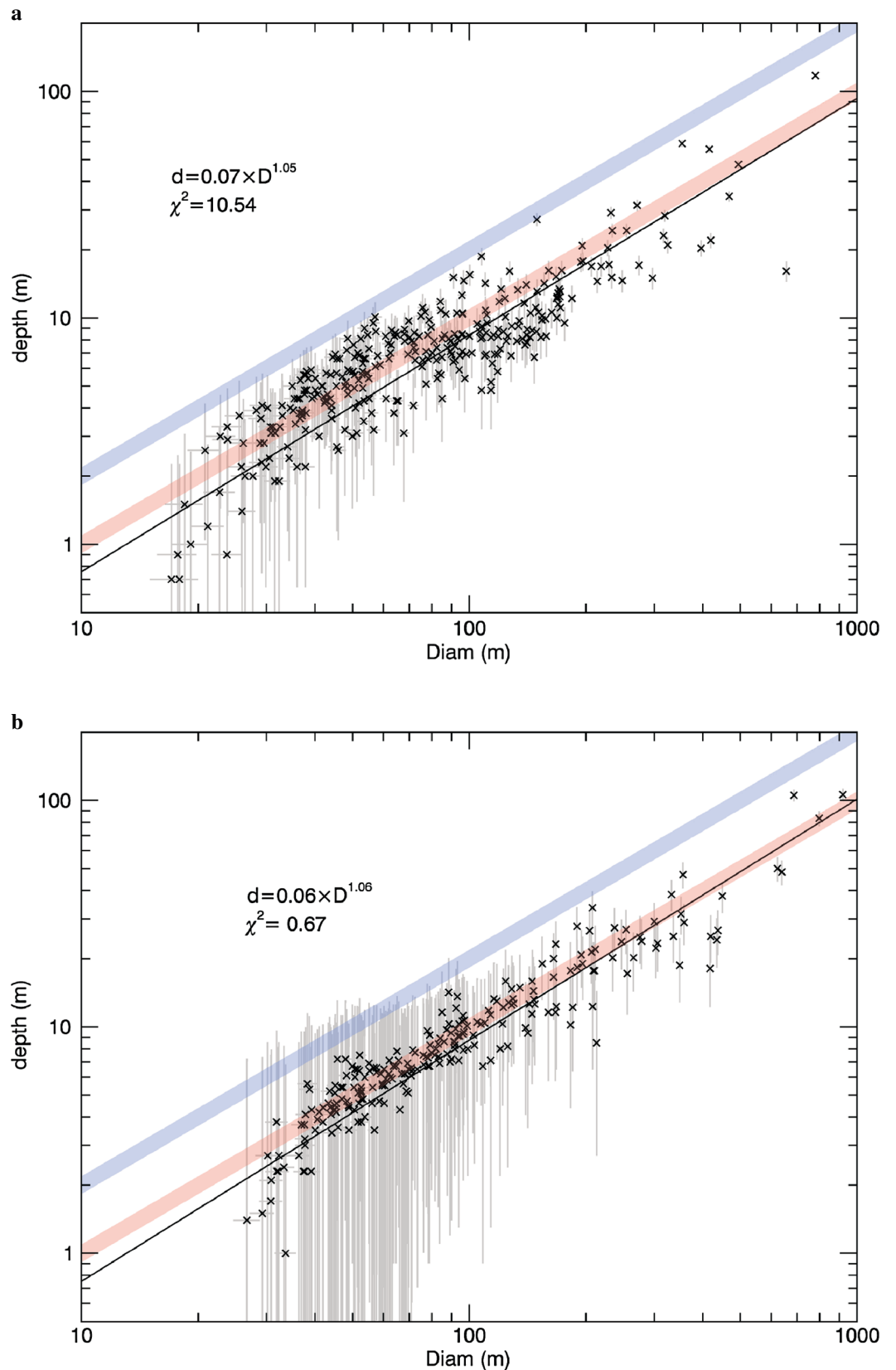


Figure 10. Lunar crater depths and diameters, plotted as in Figure 4. (a) Craters near the Apollo 15 landing site (26.06°N, 3.60°E). (b) Craters in Mare Ingenrii (−35.55°N, 164.73°E).

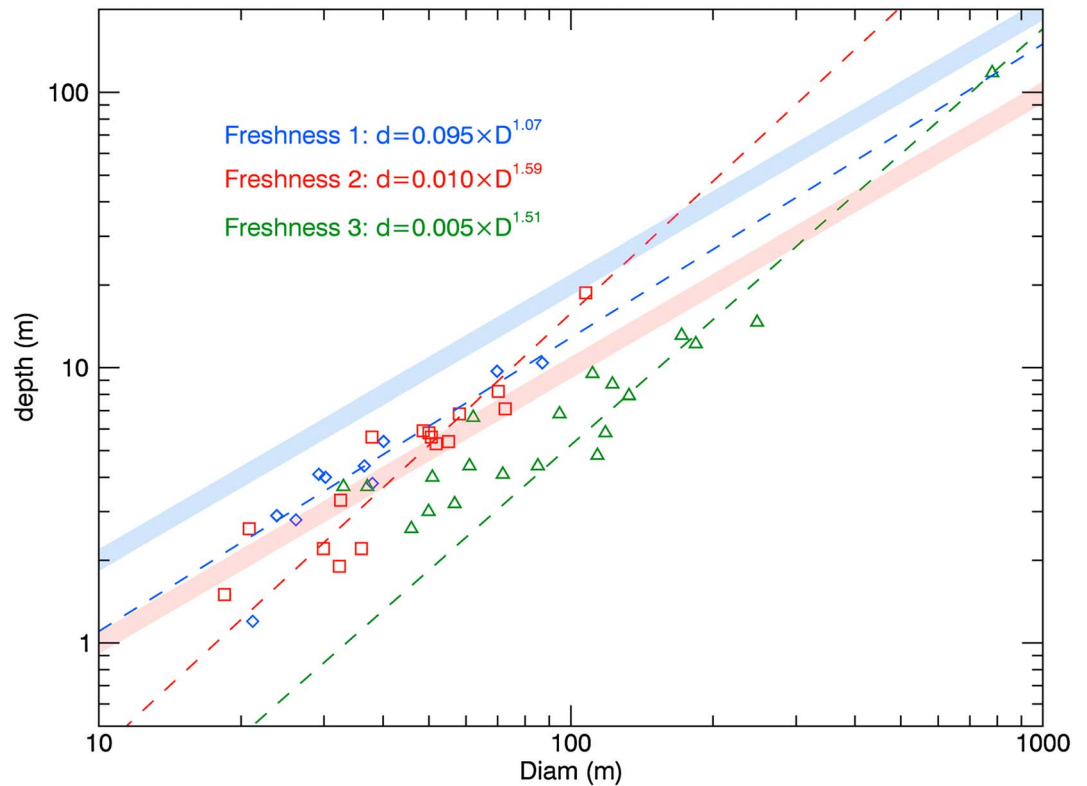


Figure 11. Values of d/D for selected lunar craters near the Apollo landing site from Figure 10a, plotted as in Figure 4. Here a subset is separated by level of apparent freshness (1 = most fresh, blue diamonds; 2 = medium fresh, red squares; 3 = least fresh, green triangles).

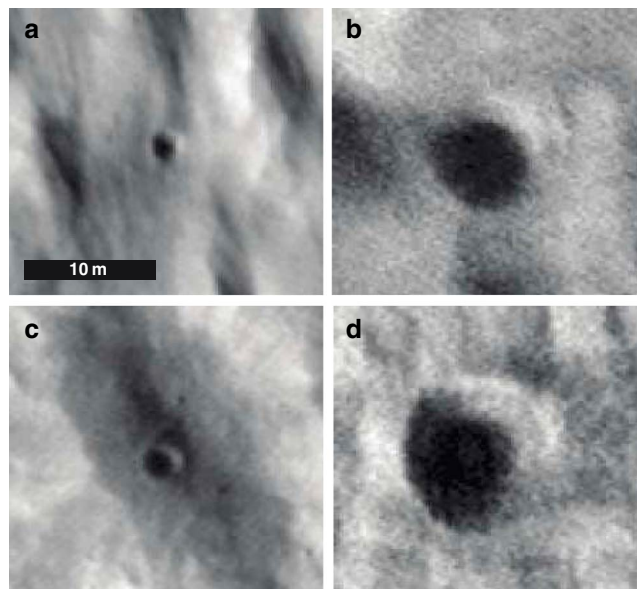


Figure 12. Examples of craters with higher values of d/D than typical for simple fresh primaries. All cutouts are at the same scale. (a) HiRISE RED RDR observation ESP_011295_2205, 40.219°N, 221.134°E, $d/D = 0.50$. (b) ESP_013267_2085, 28.425°N, 25.363°E, $d/D = 0.42$. (c) ESP_011428_2200, 38.488°N, 190.025°E, $d/D = 0.39$. (d) ESP_020487_2265, 46.042°N, 188.471°E, $d/D = 0.42$.

used on nested or concentric craters (e.g., Figure 2b), but excluding nested craters should not necessarily introduce a d/D bias.

These craters are so small (a few to tens of meters in diameter) that local topography might also be affecting their actual d/D during crater formation or its determination. We did not include craters located on obvious sloping topography, such that their outline in plan view was distorted; however, a gentle slope might not be obvious in visual images in all cases.

Measurements of d/D made from DTMs (sections 2.2 and 2.3) should not be artificially affected by local slopes; since the entire rim contour is averaged, the overall slope should cancel out.

However, a local slope could cause a distortion in measured depth when using the shadow technique (section 2.1). Figure 12c may be an example of this.

This could be either an apparent

exaggeration or underestimation of the depth, depending on slope and shadow orientations. However, with over 200 craters at 72 different sites and thus at least as many orientations, this effect would presumably average out. It could, however, be contributing to the scatter seen in our results (Figures 4–6). Topographic effects such as these should apply to secondary craters of this size as well as this set of primaries, so they may not be important in terms of a comparison between the two.

The wide range in d/D that we observe is not uncommon in craters of this scale [e.g., *Stopar et al.*, 2012; *Mahanti et al.*, 2014; *Basilevsky et al.*, 2014]. The largest Martian crater measured, with a diameter of 33 m, is quite close to the typical d/D of 0.2, but that could be a coincidence. For the smallest craters, d/D varies from less than 0.1 to more than 0.4, with a surprisingly high maximum of 0.5 in one case (Figures 5 and 12). The variation could represent different target material properties such as varying strength, porosity, or layering of targets; or impactor conditions such as impact velocity, impact angle, or physical state of the bolide (i.e., strength, fractured versus cohesive). We can eliminate variations due to different surface exposure ages or crater degradation states in the Martian craters, since they are all of known, extremely young, ages. There is a much wider range of d/D for the smallest of our craters (Figure 5).

One possible explanation for the wide distribution in d/D is that strength variations in the target have a larger effect on small craters like these. Although the transition between strength and gravity cratering regimes can span a wide range of crater diameters [e.g., *Holsapple*, 1993], the transition diameters are roughly ~90–190 m on Mars and 210–430 m on the Moon (using equations (7.5.4) and (7.7.14) from *Melosh* [1989] and a lower limit of 2 MPa for yield stress of fractured postimpact rock and experimentally determined value of 0.9 MPa for $C_{TR}Y$ in the respective equations; using a higher value for the yield stress increases the upper limit). All of the Martian craters and the majority of lunar craters (90–98% depending on the limit used) in this study are thus within the strength regime or at least in the lower range of a transitional regime where both strength and gravity play a role. In comparison, previous studies have almost all been done on larger craters in the gravity regime. If the higher d/D values we find here are robust, the cohesive strength of the material is most likely playing a role in the final morphology of these craters. Conical craters allow for d/D only up to 0.35 in unconsolidated material; higher d/D are possible if their steepest slopes exceed the angle of repose due to cohesion; or the angle of repose is steeper than that of aeolian sand due to large, angular particles, as might be expected in impact breccia.

Variations in d/D have been attributed to differences in regional terrain and material properties [e.g., *Stewart and Valiant*, 2006]. The spatial bias in our data set of new dated Martian craters makes possible a bias toward weaker materials. Specifically, these recent events all impacted areas with a uniform dust cover and, at many sites, significant dust mantling. This selection effect is a result of the detection method, which relies on low-resolution identification of surrounding dark blast zones where surface dust has been disturbed [*Malin et al.*, 2006; *Daubar et al.*, 2013]. Much of the energy of impact into a porous material goes into compaction rather than ejection of material, resulting in relatively smaller, deeper craters [*Love et al.*, 1993; *Giacomuzzo et al.*, 2007; *Housen and Holsapple*, 2012]. Most of the impactors in these cases are fairly dense [*Ivanov et al.*, 2009], especially compared to the thick surface layer of dust that can be identified by the muted morphology surrounding many of the sites. The dust deposits over most of these areas are ~0.1–2 m thick as estimated from thermal inertia and radar measurements [*Christensen*, 1986], an estimate that is supported by our observations of “nested” concentric craters showing a transition in material strength at similar depths (Figure 2b) [*Daubar and McEwen*, 2009]. In some areas of Arabia Terra, an overlying dust layer could be tens of meters thick, with wide regional variations [*Mangold et al.*, 2009]. Since these craters are so small, much of the excavation would be within such a possibly porous, low-strength surface layer.

Supporting this idea that differing terrains’ target properties are influencing the depth of craters, the d/D between separate sites varies widely (Figure 9 and Figure S1 and Table S3 in the supporting information). This variation suggests that local material strength plays a large role in the final morphology of small craters like these that are within the strength regime, although we cannot rule out contributions of impact velocity, impact angle, or impactor density.

Our overall average d/D of 0.23 is only slightly higher than most previous work on small primary craters of various sizes. With so much scatter in our data, the exclusion of extremely shallow craters and potential error measurements at these small sizes, the difference may not be statistically significant. The craters in this work are much more recent than have previously been measured, indicating that small craters seem to start

their lives close to $d/D \sim 0.2$ and then gradually get shallower, as crater topography is generally expected to become more subdued over time. A trend (usually measured for larger craters) has often been seen of deeper (higher d/D) craters at smaller diameters [e.g., *Stopar et al.*, 2012; *Gusakova et al.*, 2013], illustrating this expectation. The trend of fresher-appearing small lunar craters having larger d/D (Figure 11) supports the idea that these Martian craters are also deep because they are so young, and over time they will gradually get shallower. This degradation has been modeled as a diffusive process and the degradation rate measured for larger craters [*Forsberg-Taylor et al.*, 2004; *Fassett and Combellick*, 2014].

These extremely recent impacts are on average only 0.11 m deeper than they would be if they followed the d/D of 0.2 expected from larger (and also older) primaries. If this is statistically significant, it is unclear whether average erosion rates are high enough to explain the difference with erosional infilling of older primaries [*Golombek and Bridges*, 2000; *Golombek et al.*, 2006, 2010]. However, erosion and infilling rates of new craters may not follow long-term averages. The aeolian modification processes that reduce the depth of craters may act more efficiently on recently disturbed surfaces, before wind-mobilized material has had a chance to reach a new equilibrium [*Golombek et al.*, 2010]. Aeolian activity has been observed on surfaces recently disturbed by rover wheels [*Johnson et al.*, 2012; *Chojnacki et al.*, 2014]. However, some small (1–10 m diameter) Martian craters as old as ~ 100 ka still have $d/D \sim 0.2$ [*Golombek et al.*, 2010], suggesting that infill-causing craters to become significantly more shallow may still take a significant amount of time.

On the Moon, measured degradation rates are higher for younger craters [*Fassett and Combellick*, 2014] and craters with higher d/D (and thus steeper interior slopes) [*Basilevsky et al.*, 2014]. Any processes that could be responsible for shallower older craters on the Moon have not yet affected the brand new craters on Mars in this study, e.g., impact “gardening,” infill from ejecta of other impacts or seismic shaking [*Richardson et al.*, 2004]. The dominant degradation processes would most likely differ between the two bodies, in any case.

4.2. Comparison to Secondary Craters

Our d/D for these recent Martian primary craters are for the most part distinct from those reported for secondary craters, which have much lower d/D : 0.11 for lunar secondaries [*Schultz and Singer*, 1980] and for Martian secondaries [*McEwen et al.*, 2005]. Although some of the new craters have d/D near 0.1 (Figure 6), 64% of them have $d/D > 0.2$, so the majority would not be confused with secondaries based on their depths. However, using d/D to distinguish individual craters smaller than 30 m diameter as primaries or secondaries is problematic due to the large spread in observed values and potential for change in d/D over time if the age of the crater is unknown. Rather, it can be used as a statistical tool only.

Statistically, the d/D trends of the lunar craters follow quite closely those of typical secondaries. Not a single crater has a d/D as deep as 0.2; the maximum at each site was only 0.18 (Apollo 15) and 0.16 (Mare Ingrénii). Even these rare deeper craters may be distant secondaries, as such craters may have $d/D \sim 0.15$, perhaps as high as ~ 0.2 , on Mars [*Watters and Radford*, 2014]. The overall d/D trends we measure are similar to other studies using LROC DTMs and craters of this size range [*Stopar et al.*, 2012; *Gusakova et al.*, 2013; *Mahanti et al.*, 2014; *Basilevsky et al.*, 2014].

Although again, the specific provenance of any individual crater is difficult to determine based solely on d/D , collectively, almost all of these fresh-looking random small craters have the d/D characteristics of secondaries. However, based on d/D alone, it would be difficult to distinguish a (potentially young) set of secondaries with $d/D \sim 0.1$ from a degraded set of primaries that originally had $d/D \sim 0.2$ and had become shallower over time. Even the tight distribution around $d/D = 0.1$ does not favor the first scenario, because craters rapidly become more shallow initially [*Fassett and Combellick*, 2014; *Basilevsky et al.*, 2014]. Degradation then slows as d/D nears 0.1 [*Basilevsky et al.*, 2014], causing older primaries with different ages to cluster around $d/D = 0.1$ eventually. We do not know how likely it is that all of the lunar craters measured at these sizes are degraded primaries and none are secondaries. The relative numbers of each cannot be determined from d/D alone.

The nearly identical d/D trends among single-crater sites and clustered site support models that indicate deceleration and ablation in the present atmosphere have a negligible additional effect on fragmented impactors of these sizes when compared to unfragmented impactors [*Popova et al.*, 2003; *Williams et al.*,

2014]. These atmospheric effects must affect fragmented impactors more than intact ones; however, any additional atmospheric effects experienced by fragmented impactors are small enough that they do not measurably affect their final d/D , since we see no difference in the d/D between clusters formed by fragmented impactors and single-crater sites formed by unfragmented impactors. In addition, we see no correlation between d/D and elevation, indicating that the widely varying atmospheric density with elevation on Mars has negligible effect on final crater d/D . This may indicate a lack of correlation between impact velocity and d/D , since atmospheric deceleration must be significantly different between sites spanning 16 km of elevation, yet we see no systematic trend in d/D .

4.3. Implications for Secondary “Contamination”

How does this inform the low d/D ratios (0.11) of relatively fresh Martian craters [McEwen *et al.*, 2005]? If the d/D we measure is typical of fresh primaries on Mars, then small craters on random plains with lower $d/D \sim 0.1$ could be largely secondaries or they could be degraded primaries. If the former, the amount of distant, unrecognized secondaries at small diameters ($< \sim 50$ m) could still be quite high, depending on how long primary craters remain deeper before they are filled in. If secondaries still dominate the statistics, that would explain the discrepancy between the current rate of primary impacts (which could still be unusual over long-term geologic history) and model predictions [Neukum *et al.*, 2001; Ivanov, 2001; Hartmann, 2005] that include such unrecognized secondaries [Daubar *et al.*, 2013].

Another possibility is that the rate of crater degradation is highly nonlinear over the lifetime of a crater [e.g., Golombek and Bridges, 2000; Golombek *et al.*, 2006; Basilevsky *et al.*, 2014], such that the d/D of fresh craters with steep slopes is quickly reduced but then remains stable for a significant period of time, as Fassett and Combellick [2014] and Basilevsky *et al.* [2014] have suggested for the Moon. This could be enhanced by aeolian processes on Mars. Distinguishing between the two possibilities is not possible using d/D measurements alone. Continued monitoring of the new impact sites should provide some insights into these processes. As yet, however, topographic changes that might eventually reduce d/D have not been observed at any of the new impact sites in three Mars years of monitoring [Daubar *et al.*, 2012, 2014], indicating that these erosional/infilling processes will take an extended period of monitoring to observe. Cratering rates on the Moon and Mars are close to within a factor of two over all sizes, but at small diameters the Moon experiences as much as 2.5 times the impact rate as Mars (depending on the model used) [Ivanov, 2001]. Thus, the cumulative effects of impact gardening on small craters may be higher on the Moon. However, other erosional processes that reduce crater relief might be expected to take even longer on the Moon where aeolian and fluvial processes are absent. Estimated erosion rates on Mars vary widely and are highly dependent on assumptions made by those authors. At different sites, using different methods, estimates range from ~ 0.01 – 10^4 nm/yr over the last ~ 3.5 Gy through the present [Golombek and Bridges, 2000; Golombek *et al.*, 2006, 2014, and references therein]. However, these estimates are only valid if no impact cratering has occurred in the specified time frame, which is obviously incorrect for older surfaces. Rates on the Moon average ~ 0.2 – 0.5 nm/yr over the last ~ 3.85 Gy [Craddock and Howard, 2000; Fassett, 2013]. Although it is clear that erosive styles differ (primarily impact gardening on the Moon versus aeolian and fluvial processes on Mars), degradation rates are not known well enough to be comparable. Thus, the rate at which the d/D of craters decreases over time also cannot be compared between the two bodies, although the process must be occurring on both of them.

5. Conclusions

Meter- to decameter-scale craters at recent dated impact sites on Mars have an average depth/diameter ratio of 0.23. This is only slightly deeper than that expected for small fresh primaries based on previous studies of larger, older simple craters. These new Martian craters may be slightly deeper than older craters due to infilling of those older craters. Those processes that cause craters to become more shallow may not be linear over time, but instead be more effective over recently disturbed areas. Although this has not yet been observed in the new craters, it may be a longer-term process than the few Mars years over which we have observed them and thus require a longer period of high-resolution monitoring.

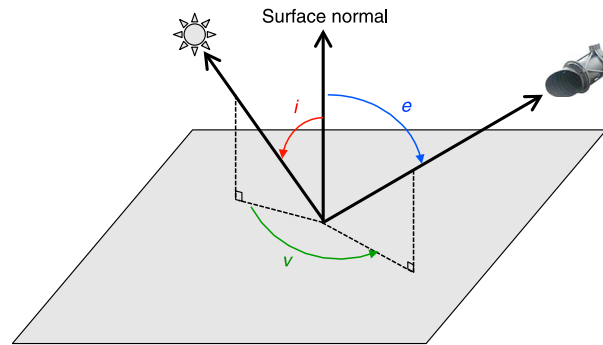


Figure A1. Definition of the photometric angles used in the discussion: i = incidence angle, angle between vector from the target to the Sun and the surface normal; e = emission angle, angle between vector from the target to the observer and the surface normal; v = angle between the subsolar point, the target, and the subspacecraft point. This is equivalent to the difference between the subsolar azimuth and the subspacecraft azimuth.

Large variations in d/D , from less than 0.1 to more than 0.4, between Martian impact sites indicate that target material properties or other details of the impact conditions may play a sizeable role in determining the depth of small craters. This also complicates identification of any one single crater or impact site as a primary or secondary based on d/D alone.

Taken as a whole data set, however, it would be difficult to mistake most of these new Martian craters for secondaries based on their morphology. Fresh craters such as these are collectively easily distinguishable as primaries. The origins of older craters are still ambiguous, though. Illustrating this, the average d/D of random small craters on the Moon is ~ 0.1 . This indicates that either the majority are

unrecognized secondary craters or some unknown proportions are primary craters degraded to similar shapes. Their d/D alone cannot distinguish between these possibilities.

Appendix A: Derivation of Azimuth Angle Correction to Shadow Measurement Technique

The original shadow measurement technique of *Chappelow and Sharpton* [2002] depends only on the incidence angle (i) of the observation and does not include any dependency on emission angle (e) or separation between the subspacecraft and subsolar azimuths (v) (these angles are defined in Figure A1). Thus, it is truly accurate only for nadir-looking observations where $e = 0^\circ$. Off-nadir observations, which are far more common for the HiRISE images used in this paper, require a correction that incorporates e and v because both of these angles cause apparent distortions in the measured shadow length.

Foreshortening or elongation due to varying emission angles was accounted for according to the derivation of *Barnouin et al.* [2012] and is reviewed here. Figure A2 shows an idealized case where $v = 180^\circ$; in other words,

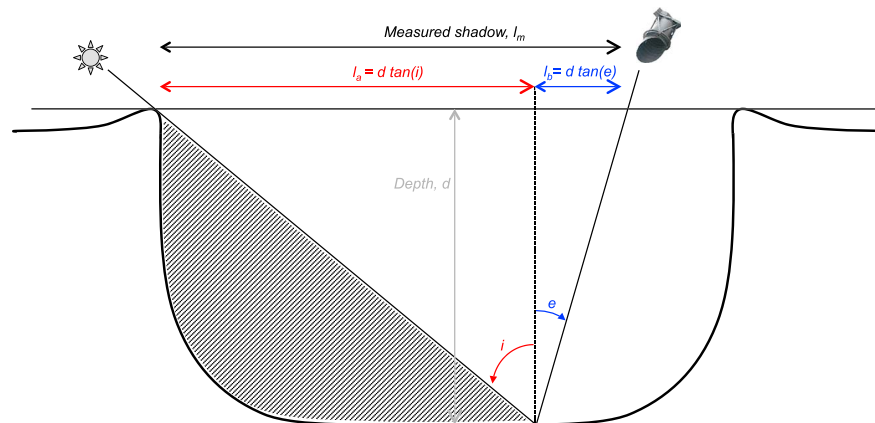


Figure A2. Cross-section schematic of flat-floored crater (not to scale), after *Barnouin et al.* [2012]. This special case shows $v = 180^\circ$, where the observer (spacecraft camera) is pointing toward the direction of the Sun, and the target, Sun, and observer are all in the same plane.

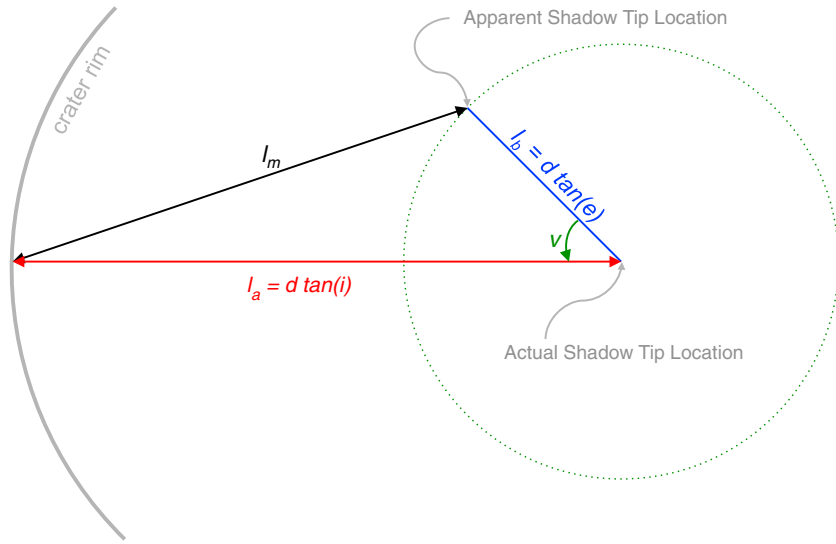


Figure A3. Plan view (not to scale) of the measured shadow length, l_m , and its components: the actual length of the shadow cast by the Sun, l_a , and the apparent displacement of the tip of this shadow, l_b , the distance of which depends on e , and the direction of which depends on v . The dotted green circle represents the trace that the shadow tip location would make if i and e were held constant and azimuth angles, v , were varied over a full 360° , lengthening or shortening l_m . The measured shadow length, l_m , is related via the cosine rule to l_a , l_b , and the angle v .

the observer (spacecraft camera) is looking toward the Sun, and the target, Sun and observer are all in the same plane. The special case where $v=0^\circ$ is similar, with the opposite sign in the formula below. The measured shadow length (l_m) is

$$l_m = l_a \pm l_b = d \tan i \pm d \tan e \tag{A1}$$

where l_a is the component of the measured shadow that is “real,” and l_b is the apparent displacement of this shadow tip (which in these two special same plane cases is along the same direction as l_a) due to the distortion caused by viewing it with a nonzero emission angle e . This correction is either positive or negative depending on whether the observer is looking toward or away from the Sun, respectively. Then,

$$d = \frac{l_m}{\tan i \pm \tan e} \tag{A2}$$

which reduces to the flat-floored crater case of *Chappelow and Sharpton* [2002] when $e=0^\circ$. This correction and analogous ones for parabolic and conical shaped craters can be found in *Barnouin et al.* [2012].

The additional correction we derive here is due to the nonideal case where the Sun, target, and observer are *not* in the same plane, i.e., $v \neq 0^\circ$ or 180° . In this case, the apparent shadow tip displacement l_b is no longer in the same direction as l_a ; instead, the shadow is also apparently distorted in length and orientation depending on the azimuth angle v . Figure A3 shows in a plan view how varying the azimuth angle v around 360° changes the direction of l_b , and thus lengthens or shortens and changes the orientation of l_m . The measured shadow length, l_m , is related to l_a ($d \tan(i)$) and l_b ($d \tan(e)$) by the cosine rule, and so it can be related to e , i , v , and d :

$$l_m^2 = l_a^2 + l_b^2 - 2l_a l_b \cos v \tag{A3}$$

or

$$l_m = d \sqrt{\tan^2 i + \tan^2 e - 2 \tan i \tan e \cos v} \tag{A4}$$

This correction has its maximum effect when $v=0^\circ$ or 180° , when foreshortening or elongation due to nonzero emission angle is at its highest. In typical situations, where $i \gg e$, shadow length is the least distorted when v is close to 90° . This correction has the advantage of being independent of the sign of v since the cosine is symmetrical, so the absolute value of the difference between the subsolar azimuth and the spacecraft azimuth can simply be used for v .

Inserting this correction into the original *Chappelow and Sharpton* [2002] results for the three shapes of craters leads to these corrected formulae:

Flat floored

$$d = \frac{l_m}{\sqrt{\tan^2 i + \tan^2 e - 2 \tan i \tan e \cos v}} \quad (\text{A5})$$

Parabolic

$$d = \frac{D}{4(1 - l_m/D) \sqrt{\tan^2 i + \tan^2 e - 2 \tan i \tan e \cos v}} \quad (\text{A6})$$

Conical

$$d = \frac{l_m}{2(1 - l_m/D) \sqrt{\tan^2 i + \tan^2 e - 2 \tan i \tan e \cos v}} \quad (\text{A7})$$

These differ from the corrections made by *Barnouin et al.* [2012] by the correction for azimuth angle v in the denominator. Note that there is a typo in the correction for conical craters *Barnouin et al.* [2012] present (their equivalent to equation (A7)): instead of D , the numerator should be l_m (O. Barnouin, personal communication, 2013).

Acknowledgments

We thank the HiRISE operations staff for acquiring the many excellent images used in this study. Thanks to Sarah Mattson and Aaron Kilgallon for producing high-quality DTMs from those data, and to Thanh Tran and Kyle Burns for the LROC NAC DTMs. Sarah Mattson and Rod Heyd were very helpful in answering questions about HiRISE data. Matthew Golombek's comments enhanced this manuscript. Olivier Barnouin kindly helped clarify his correction to the shadow measurement technique and provided a very helpful review along with Robert Herrick, both of whose feedback greatly improved this paper. We also thank JGR Editor Gareth Collins for his valuable suggestions. All LROC and HiRISE data used in this paper are publicly available on the Planetary Data System (<http://pds.jpl.nasa.gov/>). This work was funded by the NASA Mars Reconnaissance Orbiter and Lunar Reconnaissance Orbiter projects.

References

- Allen, C. C. (1979), Large lunar secondary craters—Size-range relationships, *Geophys. Res. Lett.*, *6*, 51–54, doi:10.1029/GL006i001p00051.
- Atwood-Stone, C., and A. S. McEwen (2013), Avalanche slope angles in low-gravity environments from active Martian sand dunes, *Geophys. Res. Lett.*, *40*, 2929–2934, doi:10.1002/grl.50586.
- Baldwin, R. B. (1985), Relative and absolute ages of individual craters and the rate of infalls on the Moon in the post-imbricium period, *Icarus*, *61*, 63–91.
- Banks, M. E., S. Byrne, K. Galla, A. S. McEwen, V. J. Bray, C. M. Dundas, K. E. Fishbaugh, K. E. Herkenhoff, and B. C. Murray (2010) Crater population and resurfacing of the Martian north polar layered deposits, *J. Geophys. Res.*, *115*, E08006, doi:10.1029/2009JE003523.
- Barnouin, O. S., C. E. Ernst, J. T. Heinick, S. Sugita, M. J. Cintala, D. A. Crawford, and T. Matsui (2011), Experimental results investigating the impact velocity effects on crater growth and the transient crater diameter-to-depth ratio, *42th Lunar Planet. Sci. Conf.*, Abstract 2258.
- Barnouin, O. S., M. T. Zuber, D. E. Smith, G. A. Neumann, R. R. Herrick, J. E. Chappelow, S. L. Murchie, and L. M. Prockter (2012), The morphology of craters on Mercury: Results from MESSENGER flybys, *Icarus*, *219*, 414–427, doi:10.1016/j.icarus.2012.02.029.
- Basilevsky, A. T., M. A. Kreslavsky, I. P. Karachevtseva, and E. N. Gusakova (2014), Morphometry of small impact craters in the Lunokhod-1 and Lunokhod-2 study areas, *Planet. Space Sci.*, *92*, 77–87, doi:10.1016/j.pss.2013.12.016.
- Bray, V. J., and P. M. Schenk (2014), Pristine impact crater morphology on Pluto—Expectations for new horizons, *Icarus*, doi: 10.1016/j.icarus.2014.05.005, in press.
- Calef, F. J., R. R. Herrick, and V. L. Sharpton (2009), Geomorphic analysis of small rayed craters on Mars: Examining primary versus secondary impacts, *J. Geophys. Res.*, *114*, E10007, doi:10.1029/2008JE003283.
- Chappelow, J. (2013), Simple impact crater shape determination from shadows, *Meteorit. Planet. Sci.*, *1872*(10), 1863–1872, doi:10.1111/maps.12201.
- Chappelow, J. E. (2014), The shapes of the Linne simple impact craters on the Moon—Not parabolic, *Lunar and Planetary Science Conference* 45, abstract 2074.
- Chappelow, J. E., and V. L. Sharpton (2002), An improved shadow measurement technique for constraining the morphometry of simple impact craters, *Meteorit. Planet. Sci.*, *37*, 479–486.
- Chojnacki, M., J. Johnson, T. Michaels, L. Fenton, and J. Moersch (2014), Persistent aeolian activity at endeavour crater, Meridiani Planum, Mars; New observations from orbit and the surface, *45th Lunar Planet. Sci. Conf.*, Abstract 2775.
- Christensen, P. R. (1986), Regional dust deposits on Mars—Physical properties, age, and history, *J. Geophys. Res.*, *91*, 3533–3545, doi:10.1029/JB091iB03p03533.
- Cintala, M. J., and P. J. Mouginiis-Mark (1980), Martian fresh crater depths: More evidence for subsurface volatiles?, *Geophys. Res. Lett.*, *7*, 329–332, doi:10.1029/GL007i005p00329.
- Craddock, R. A., and A. D. Howard (2000), Simulated degradation of lunar impact craters and a new method for age dating farside mare deposits, *J. Geophys. Res.*, *105*, 20,387–20,402, doi:10.1029/1999JE001099.
- Daubar, I., and A. S. McEwen (2009), Depth to diameter ratios of new Martian craters from HiRISE images, *AAS/Division for Planet. Sci. Meeting 41*, Abstract #35.08.
- Daubar, I. J., P. E. Geissler, A. S. McEwen, C. M. Dundas, and S. Byrne (2012) Repeat observations of new impact sites on Mars: Changes in blast zones, *AGU Fall Meeting Abstracts*.
- Daubar, I. J., A. S. McEwen, S. Byrne, M. R. Kennedy, and B. Ivanov (2013), The current Martian cratering rate, *Icarus*, *225*, 506–516, doi:10.1016/j.icarus.2013.04.009.
- Daubar, I. J., P. E. Geissler, A. S. McEwen, C. M. Dundas, S. Byrne, P. S. Russell, and G. D. Bart (2014), Changes in new impact blast zones over three Martian years, *45th Lunar Planet. Sci. Conf.*, Abstract 2762.
- Fassett, C. I. (2013), Crater degradation of kilometer-sized craters on the lunar maria: Initial observations and modeling, *Lunar Planet. Sci. Conf.*, Abstract 2026.
- Fassett, C. I., and J. R. Combellick (2014), The rate of crater degradation and topographic evolution on the Moon: Results from the maria and initial comparisons with the highlands, *45th Lunar Planet. Sci. Conf.*, Abstract 1429.

- Forsberg-Taylor, N. K., A. D. Howard, and R. A. Craddock (2004), Crater degradation in the Martian highlands: Morphometric analysis of the Sinus Sabaeus region and simulation modeling suggest fluvial processes, *J. Geophys. Res.*, *109*, E05002, doi:10.1029/2004JE002242.
- Garvin, J. B., S. E. H. Sakimoto, and J. J. Frawley (2003), Craters on Mars: Global geometric properties from gridded MOLA topography, *Sixth Int. Conf. on Mars*, Abstract 3277.
- Giacomuzzo, C., F. Ferri, A. Bettella, D. Pavarin, A. Francesconi, E. Flamini, and F. Angrilli (2007), Hypervelocity experiments of impact cratering and catastrophic disruption of targets representative of minor bodies of the Solar System, *Adv. Space Res.*, *40*, 244–251.
- Golombek, M. P., and N. T. Bridges (2000), Erosion rates on Mars and implications for climate change: Constraints from the Pathfinder landing site, *J. Geophys. Res.*, *105*, 1841–1854, doi:10.1029/1999JE001043.
- Golombek, M. P., et al. (2006), Erosion rates at the Mars Exploration Rover landing sites and long-term climate change on Mars, *J. Geophys. Res.*, *111*, E12S10, doi:10.1029/2006JE002754.
- Golombek, M., K. Robinson, A. McEwen, N. Bridges, B. Ivanov, L. Tornabene, and R. Sullivan (2010), Constraints on ripple migration at Meridiani Planum from Opportunity and HiRISE observations of fresh craters, *J. Geophys. Res.*, *115*, E00F08, doi:10.1029/2010JE003628.
- Golombek, M. P., N. H. Warner, V. Ganti, M. P. Lamb, T. J. Parker, R. L. Fergason, and R. Sullivan (2014), Small crater modification on meridiani planum and implications for erosion rates and climate change on Mars, *J. Geophys. Res. Planets*, doi:10.1002/2014JE004658.
- Gusakova, E. N., A. T. Basilevsky, M. A. Kreslavsky, and I. P. Karachevtseva (2013), Morphometry of small impact craters in the Lunokhod 1 study area, *44th Lunar Planet. Sci. Conf.*, Abstract 1174.
- Hartmann, W. K. (2005), Martian cratering 8: Isochron refinement and the chronology of Mars, *Icarus*, *174*, 294–320.
- Hartmann, W. K. (2007), Martian cratering 9: Toward resolution of the controversy about small craters, *Icarus*, *189*, 274–278.
- Hartmann, W. K., C. Quantin, S. C. Werner, and O. Popova (2010), Do young Martian ray craters have ages consistent with the crater count system?, *Icarus*, *208*(2), 621–635, doi:10.1016/j.icarus.2010.03.030.
- Herrick, R. (2013), The shapes of simple craters in the outer solar system determined with an enhanced shadow measurement technique, *44th Lunar Planet. Sci. Conf.*, Abstract 7320.
- Holsapple, K. A. (1993), The scaling of impact processes in planetary sciences, *Annu. Rev. Earth Planet. Sci.*, *21*, 333–373, doi:10.1146/annurev.ea.21.050193.002001.
- Housen, K. R., and K. A. Holsapple (2012), Craters without ejecta, *Icarus*, *219*(1), 297–306, doi:10.1016/j.icarus.2012.02.030.
- Ivanov, B. A. (2001), Mars/Moon cratering rate ratio estimates, *Space Sci. Rev.*, *96*, 87–104.
- Ivanov, B. A., H. J. Melosh, A. S. McEwen, and HiRISE Team (2009), Small impact crater clusters in high resolution HiRISE images—II, *40th Lunar Planet. Sci. Conf.*, Abstract 1410.
- Johnson, J. R., J. F. Bell III, R. E. Arvidson, and J. A. Herman (2012), Surface changes observed at Greeley Haven during Opportunity's fifth Martian winter, *AGU Fall Meeting abstracts*.
- Kirk, R. L., E. Howington-Kraus, B. Redding, D. Galuszka, T. M. Hare, B. A. Archinal, L. A. Soderblom, and J. M. Barrett (2003), High-resolution topomapping of candidate MER landing sites with Mars Orbiter Camera narrow-angle images, *J. Geophys. Res.*, *108*(12), 8088, doi:10.1029/2003JE002131.
- Kirk, R. L., et al. (2008), Ultrahigh resolution topographic mapping of Mars with MRO HiRISE stereo images: Meter-scale slopes of candidate Phoenix landing sites, *J. Geophys. Res.*, *113*, E00A24, doi:10.1029/2007JE003000.
- Love, S. G., F. Hörz, and D. E. Brownlee (1993), Target porosity effects in impact cratering and collisional disruption, *Icarus*, *105*, 216–224.
- Mahanti, P., M. Robinson, R. Stelling, S. J. Lawrence, and J. Stopar (2013), A probabilistic model to explore depth-diameter dependencies for lunar craters, *44th Lunar Planet. Sci. Conf.*, Abstract 1215.
- Mahanti, P., M. S. Robinson, and R. Stelling (2014), How deep and steep are small lunar craters? New insights from LROC NAC DEMs, *45th Lunar Planet. Sci. Conf.*, Abstract 1584.
- Malin, M. C., K. S. Edgett, L. V. Posiolova, S. M. McColley, and E. Z. N. Dobra (2006), Present-day impact cratering rate and contemporary gully activity on Mars, *Science*, *314*, 1573–1577, doi:10.1126/science.1135156.
- Malin, M. C., et al. (2007), Context Camera investigation on board the Mars Reconnaissance Orbiter, *J. Geophys. Res.*, *112*, E05S04, doi:10.1029/2006JE002808.
- Mangold, N., V. Ansan, P. Masson, and C. Vincendon (2009), Estimate of the aeolian dust thickness in Arabia Terra, Mars: Implications of a thick mantle (20 m) for hydrogen detection, *Géomorphol. Relief, Processus, Environ.*, *1*, 23–32.
- Mattson, S., R. L. Kirk, R. Heyd, A. S. McEwen, E. Eliason, T. Hare, R. Beyer, E. Howington-Kraus, C. Okubo, and K. Herkenhoff (2011), Release of HiRISE digital terrain models to the planetary data system, *42th Lunar Planet. Sci. Conf.*, Abstract 1558.
- McEwen, A. S., and E. B. Bierhaus (2006), The importance of secondary cratering to age constraints on planetary surfaces, *Ann. Rev. Earth Planet. Sci.*, *34*, 535–567.
- McEwen, A. S., B. S. Preblich, E. P. Turtle, N. A. Artemieva, M. P. Golombek, M. Hurst, R. L. Kirk, D. M. Burr, and P. R. Christensen (2005), The rayed crater Zunil and interpretations of small impact craters on Mars, *Icarus*, *176*, 351–381.
- McEwen, A. S., et al. (2007), Mars Reconnaissance Orbiter's High Resolution Imaging Science Experiment (HiRISE), *J. Geophys. Res.*, *112*, E05S02, doi:10.1029/2005JE002605.
- Melosh, H. J. (1989), *Impact Cratering: A Geologic Process*, *Oxford Monogr. on Geol. and Geophys.*, vol. 11, pp. 253, Oxford Univ. Press, New York.
- Neukum, G., B. A. Ivanov, and W. K. Hartmann (2001), Cratering records in the inner solar system in relation to the lunar reference system, *Space Sci. Rev.*, *96*, 55–86.
- Pike, R. (1974), Depth/diameter relations of fresh lunar craters: Revision from spacecraft data, *Geophys. Res. Lett.*, *1*, 291–294, doi:10.1029/GL001i007p00291.
- Pike, R. J. (1977), Apparent depth/apparent diameter relation for lunar craters, *Proc. Lunar Planet. Sci. Conf.*, *8*, 3427–3436.
- Pike, R. J. (1980), Control of crater morphology by gravity and target type—Mars, Earth, Moon, *Proc. Lunar Planet. Sci. Conf.*, *11*, 2159–2189.
- Pike, R. J., and D. E. Wilhelms (1978), Secondary-impact craters on the Moon: Topographic form and geologic process, *Lunar Planet. Inst. Sci. IX*, 907–909 (abstract).
- Popova, O., I. Nemtchinov, and W. K. Hartmann (2003), Bolides in the present and past Martian atmosphere and effects on cratering processes, *Meteorit. Planet. Sci.*, *38*, 905–925, doi:10.1111/j.1945-5100.2003.tb00287.x.
- Popova, O. P., W. K. Hartmann, I. V. Nemtchinov, D. C. Richardson, and D. C. Berman (2007), Crater clusters on Mars: Shedding light on Martian ejecta launch conditions, *Icarus*, *190*, 50–73, doi:10.1016/j.icarus.2007.02.022.
- Richardson, J. E., H. J. Melosh, and R. Greenberg (2004), Impact-induced seismic activity on asteroid 433 Eros: A surface modification process, *Science*, *306*, 1526–1529, doi:10.1126/science.1104731.
- Robinson, M. S., et al. (2010), Lunar Reconnaissance Orbiter Camera (LROC) instrument overview, *Space Sci. Rev.*, *150*, 81–124, doi:10.1007/s11214-010-9634-2.

- Ruff, S. W., and P. R. Christensen (2002), Bright and dark regions on Mars: Particle size and mineralogical characteristics based on Thermal Emission Spectrometer data, *J. Geophys. Res.*, *107*(E12), 5119, doi:10.1029/2001JE001580.
- Schultz, P. H. (1989), Cratering on Mercury—A relook, in *Mercury*, edited by F. Vilas, C. R. Chapman, and M. S. Matthews, pp. 274–335, Univ. of Arizona Press, Tuscon, Ariz.
- Schultz, P. H., and J. Singer (1980), A comparison of secondary craters on the moon, Mercury, and Mars, *Proc. Lunar Planet. Sci. Conf.*, *11*, 2243–2259.
- Shoemaker, E. M. (1965), Preliminary analysis of the fine structure of the lunar surface in Mare Cognitum, JPL Tech. Report No. 32–700, in *The Nature of the Lunar Surface*, edited by W. N. Hess, D. H. Menzel, and J. A. O'Keefe, pp. 23–77, Johns Hopkins Press, Baltimore, Md.
- Stewart, S. T., and G. J. Valiant (2006), Martian subsurface properties and crater formation processes inferred from fresh impact crater geometries, *Meteorit. Planet. Sci.*, *41*, 1509–1537, doi:10.1111/j.1945-5100.2006.tb00433.x.
- Stopar, J., M. Robinson, E. J. Speyerer, K. Burns, H. Gengl, and the LROC Team (2012), Regolith characterization using LROC NAC digital elevation models of small lunar craters, *43th Lunar Planet. Sci. Conf.*, Abstract 2729.
- Tornabene, L. L., J. E. Moersch, H. Y. McSween Jr., A. S. McEwen, J. L. Piatek, K. A. Milam, and P. R. Christensen (2006) Identification of large, 2–10 km. rayed craters on Mars in THEMIS thermal infrared images: Implications for possible Martian meteorite source regions, *J. Geophys. Res.*, *111*, E10006, doi:10.1029/2005JE002600.
- Watters, W., and A. Radford (2014), 3-D morphometry of Martian secondary impact craters from Zunil and Gratteri, *45th Lunar Planet. Sci. Conf.*, Abstract 2836.
- Wells, K. S., D. B. Campbell, B. A. Campbell, and L. M. Carter (2010), Detection of small lunar secondary craters in circular polarization ratio radar images, *J. Geophys. Res.*, *115*, E06008, doi:10.1029/2009JE003491.
- Wilcox, B. B., M. S. Robinson, P. C. Thomas, and B. R. Hawke (2005), Constraints on the depth and variability of the lunar regolith, *Meteorit. Planet. Sci.*, *40*(5), 695–710, doi:10.1111/j.1945-5100.2005.tb00974.x.
- Williams, J.-P., A. V. Pathare, and O. Aharonson (2014), The production of small primary craters on Mars and the Moon, *Icarus*, *235*, 23–36, doi:10.1016/j.icarus.2014.03.011.
- Wood, C. A., and L. Anderson (1978), New morphometric data for fresh lunar craters, *Lunar Planet. Sci. Conf. Proc.*, *9*, 3669–3689.